Microstructure, local and global mechanical properties of friction stir welds in aluminium alloy 6005A-T6

Aude Simar, Yves Bréchet, B. de Meester, Anne Denquin, Thomas Pardoen

Microstructure, local and global mechanical properties of friction stir welds in aluminium alloy 6005A-T6

A. Simar [a,b,*], Y. Bréchet [c], B. de Meester [a], A. Denquin [d], T. Pardoen [b]

[a] *Département de Mécanique, Université catholique de Louvain, PRM, Place du Levant 2, B-1348 Louvain-la-Neuve, Belgium*
[b] *Département des Sciences des Matériaux et des Procédés, Université catholique de Louvain, IMAP, Place Sainte Barbe 2, B-1348 Louvain-la-Neuve, Belgium*
[c] *LTPCM/INPG, CNRS UMR 5614, Domaine Universitaire, BP 75, 38402 Saint Martin d'Hères, France*
[d] *Office National d'Etudes et de Recherches Aérospatiales, 29 avenue de la Division Leclerc, 92322 Châtillon Cedex, France*

The effect of the welding speed on the microstructure, local and overall mechanical properties of friction stir welded joints has been investigated in the aluminium alloy 6005A-T6. The fine hardening precipitation within the heat-affected zone has been characterized by differential scanning calorimetry (DSC) and transmission electron microscopy (TEM). Post-welding heat treatments have been applied to obtain indications on the level of solid solution supersaturation in the as welded state. The local mechanical behaviour was determined using thin specimens extracted from various regions of the weld. The overall properties were measured on samples cut perpendicular to the weld. Specific attention was devoted to the relationship between the local microstructure and local hardening properties in the weakest region, which govern the overall strength and ductility of the welds.

Keywords: Friction stir welding; Tensile test; Differential scanning calorimetry (DSC); Transmission electron microscopy (TEM); Aluminium alloys; Precipitation

1. Introduction

Friction stir welding technology (FSW), although relatively new [1], is already used to assemble aluminium panels in several industrial applications. However, many aspects of the microstructure evolution during the welding process and of its effect on the local and global mechanical properties are still poorly understood. For instance, complex issues related to the localization of plastic deformation and damage evolution, controlling the formability and fracture resistance still need to be understood with respect to the heterogeneous local mechanical properties induced by the process. Hence, while there is no doubt that the FSW process is adequate for welding secondary structural components, the optimized design of primary structural components with adequate fracture toughness and the success of post-welding forming operations requires a better understanding of the process–microstructure–properties relationships. The purpose of this work is to provide the experimental database from which a fully integrated modelling strategy, spanning microstructure to the end use properties, can be motivated and validated. Specific attention will be devoted to the strain hardening behaviour of the weld regions, which controls both the strength and resistance to plastic localization. The investigation has been performed on an AA6005A extrusion alloy, which presents a potential for FSW applications.

The basics of the FSW process are recalled first (see Fig. 1). The plates to be welded are rigidly clamped on a table. A rotating tool pin penetrates into the material until the tool shoulder contacts with the upper surface of the plates. The weld is asymmetric since on one side of the weld, called the advancing side, the rotation of the tool is in the direction of the advancing velocity, while on the other side, called the retreating side, it is moving in the opposite direction. As a general convention for all the figures proposed in this paper, the advancing side of the weld will correspond to the left hand side, i.e. a position $y < 0$. The resulting friction stir welding joint consists of several zones involving different microstructures and mechanical properties. The heat-affected zone (HAZ) is the furthest away from the joint line and experiences little or no deformation, but is still influenced by the heat generated by the process which affects the microstructure, generally through the growth of the precipitates originally present. The thermo-mechanically affected zone (TMAZ) is closer to the weld centre

* Corresponding author at: Département de Mécanique, Université catholique de Louvain, PRM, Place du Levant 2, B-1348 Louvain-la-Neuve, Belgium.
E-mail address: aude.simar@uclouvain.be (A. Simar).

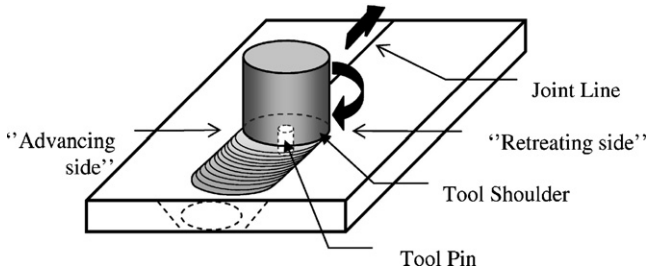

Fig. 1. Principle of the friction stir welding process (from Ref. [19]).

and is both highly deformed and subjected to a heating and cooling sequence. At the level of the tool itself, the so-called "nugget" undergoes intense deformation and heating leading to a recrystallized microstructure made of very fine grains [2,3].

The AA6005A alloy investigated in this work has low copper and low excess silicon content (see Table 1). The hardening phases are the metastable precursors of the stable Mg_2Si phase. The generally accepted precipitation sequence is the following [4–7]: supersaturated solid solution $\rightarrow$ clusters/GP zones $\rightarrow \beta'' \rightarrow \beta' + B' + Si + (\text{Type A and B}) \rightarrow \beta\ (Mg_2\ Si) + Si$. The GP zones are produced during low temperature or even room temperature aging. The precipitates β'' are fully coherent needle-shaped precipitates, formed in particular during the artificial aging heat treatment T6, and responsible for the peak hardness when their size is optimum. The semi- or non-coherent precipitates following β'' in the precipitation sequence and corresponding to overaging conditions have a much lower hardening potential [7]. The rod-shaped β' precipitates are semi-coherent, while the B' precipitates are lath-like with a rectangular cross-section. Silicon-rich precipitates can also arise in the precipitation sequence due to the excess silicon in the alloy. Finally, during the casting of industrial aluminium of the 6xxx series, the presence of other residual elements can lead to intermetallic inclusions, which are iron-rich with a typical size ranging between 1 and 10 μm and responsible for the nucleation of damage by plastic deformation (e.g. Gallais et al. [8], and Lassance et al. [9]), in addition to dispersoïds with a size on the order of 100 nm, which are manganese and/or chromium-rich particles controlling grain growth.

Sato et al. [10] studied the evolution of the hardening precipitates in a 6063-T5 friction stir weld by TEM observations. The base material has a large fraction of needle-shaped precipitates while the heat-affected medium hardness zone showed fewer needle-shaped precipitates, but also rod-shaped precipitates. The region of minimum hardness within the heat-affected zone involved a low density of large rod-shaped precipitates. In the central zone of the weld, all the precipitates were dissolved. Lee et al. [11] obtained similar conclusions from TEM observation of a 6005-T6 FSW. The needle-shaped precipitates have been identified as β'' precipitates and the rod-shaped precipitates as β' precipitates. Sato et al. [12] showed that a post-weld heat treatment on a 6063-T5 friction stir weld forces the precipitation of β'' phases in regions where the magnesium and silicon is in solid solution.

Table 1
Chemical composition of aluminium alloy 6005A (wt%)

Al	98.18
Si	0.81
Mg	0.48
Fe	0.24
Mn	0.11
Cu	0.09
Zn	0.07
Ti	0.02

The characterization of the flow properties of the different zones of friction stir welds is usually made by microhardness mapping measurements. A few authors have worked on more quantitative mechanical methods, e.g. [8,13–19]. Von Strombeck et al. [13] extracted tensile specimens from the different zones of a 6061-T6 friction stir weld. The ultimate tensile strength of the weld centre was larger than that of the heat-affected zone while the yield strength was similar. Conclusions about the variations of the fracture strain are more difficult to draw from these studies because of differences in the definition of the fracture strain, taken sometimes as the strain at maximum load or the strain at the actual fracture based on the final elongation expressed either in true or engineering terms. Nevertheless, the general trend is that the fracture strain of the weld central region is lower than the fracture strain of the base material if the base material is in the T4 or in the T6 state. Usually, plastic deformation localization takes place in the zone of lowest hardness. As a general conclusion, the overall flow and fracture properties of friction stir welds seem to be highly dependent on the behaviour of the weakest zone.

The outline of the paper is the following. The experimental procedures for the characterization of the microstructure and for the measurement of the mechanical properties of the welds will be presented in the following section followed by a description of the model used to simulate the response of a welded joint from the local mechanical properties. The results of the characterizations and FE simulations are given in Section 4 with a specific attention devoted to the description of the DSC measurements and to the distribution of local tensile properties throughout the different zones. The final discussion in Section 5 aims at linking the microstructure evolution in the welds, the local tensile properties in the different zones of the welds and the global mechanical properties, as well as the effect of the advancing speed.

2. Materials and experimental procedure

2.1. Base material

The base material addressed in this study is a 6 mm thick 6005A aluminium alloy delivered in a T6 state with the chemical composition given in Table 1.

2.2. Weld production

Friction stir welds have been produced on a Hermle 3-axis CNC milling machine. During welding, thermocouples provided the thermal history at various distances away from the weld centreline. The results of these measurements have been

reported elsewhere [20]. The welding direction is parallel to the extrusion direction. Two specific welding conditions were investigated in detail: a "hot" weld with an advancing speed of 200 mm/min and a rotational speed of 1000 rpm and a "cold" weld with the same rotational speed but with an advancing speed of 1000 mm/min. The definition of "hot" and "cold" weld refers to the advance per revolution: assuming a constant torque, a lower advance per revolution implies a higher energy (heat) input per unit length of weld. Indeed in such a case, higher peak temperatures are measured in the heat-affected zone at some distance from the weld centreline. This however does not imply that the peak temperatures in the nugget and under the tool shoulder are very different [20].

2.3. Microstructure characterization

The fine-scale hardening precipitates were observed on sections parallel to the welding line by transmission electron microscopy (TEM). The sections were first machined and manually polished down to a thickness of 100 μm. The final thickness reduction was obtained by electro-polishing with a HNO_3 solution (HNO_3 30% in volume in methanol at −30 °C under 9 V). The mean radius and length of the precipitates were determined by image analysis performed on $[0\,0\,1]_{Al}$ zone axis orientation. Differential scanning calorimetry (DSC) measurements have been performed on samples extracted at various distances from the weld centreline of the cold weld using a TA instrument MDSC 2920 apparatus. The heating rate was constant and equal to 20 °C/min.

2.4. Mechanical properties

All mechanical tests were performed either on the base material or on welded samples at least 1 year after welding in order to account for natural aging effects and to compare stabilized microstructures. Vickers 1 kg hardness tests were performed on the transverse section of the welds at various distances from the weld centre. The hardness distribution of post-welding heat-treated samples (6 h at 185 °C followed by water-quenching [21]) was also measured. Three types of tensile tests were performed on a universal ZWICK 50 kN machine.

- Tensile tests on the base material were performed both in the extrusion and long transverse direction in order to quantify the anisotropy of the mechanical properties. The material dispersion was evaluated by repeating the tests three times. The samples were 6 mm thick, 12.5 mm wide and 140 mm long, with an initial gauge length of 45 mm.
- Tensile tests on welded specimens were performed in the long transverse direction, i.e. perpendicular to the welding direction, with dimensions similar to those used for the base material. Due to inhomogeneous local deformations, only pseudo-engineering tensile properties can be determined. Furthermore, the yield strength of a weld is difficult to define since plasticity initiates in a very confined region. Hence, the yield strength of the welds was defined at 0.1% of offset to linearity. The position of fracture with respect to the weld centreline was identified using marks made on the samples prior to testing. Digital image correlation (DIC) was performed on the transverse section of the welds in order to determine in-plane strain maps during tensile testing. For those tests, the transverse section of the tensile specimens was initially painted in white with small black dots.
- Micro-tensile specimens were extracted from the different zones of the weld at positions selected on the basis of the hardness measurements and the macrographic observations of the deformed zone. The loading direction of these micro-samples corresponded to the welding direction. Fig. 2 presents a schematic of the micro-tensile samples extraction. Due to the inclination of the welded zones with equal hardness, some samples had to be machined at specific angles with respect to the axis normal to the plate. The specimens were machined very thin (0.8 mm) in order to ensure relatively homogenous properties, and were 4 mm wide and 60 mm long. The initial gauge length was equal to 30 mm.

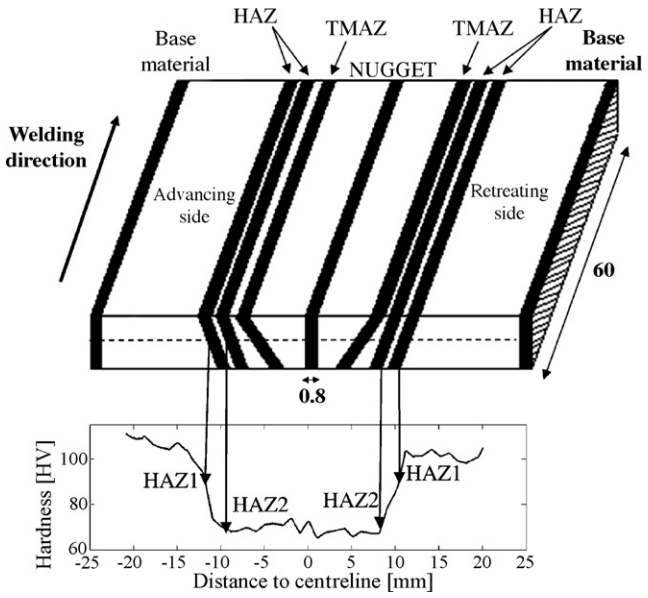

Fig. 2. Schematic on top: micro-tensile samples position of extraction (in bold black). The welding direction corresponds to the extrusion direction of the plates. The dotted line indicates the long transverse direction taken at mid-thickness of the transverse section. Graph on bottom: hardness as a function of the distance to the weld centreline in the long transverse direction at mid-thickness for the cold weld (1000 mm/min and 1000 rpm). HAZ1 corresponds to a hardness of 90 HV, HAZ2 corresponds to the lowest hardness. The samples extracted in the heat-affected zone (HAZ) and thermo-mechanically affected zone (TMAZ) are extracted in bias in order to account for the inclination with depth (transverse short direction) of the iso-hardness lines.

The plastic flow and fracture parameters identified from the tensile tests are

- the yield strength σ_y (or R_p the engineering yield strength);
- the true strain at necking ε_u (or e_u the engineering ultimate tensile strain);
- the ultimate tensile strength σ_u (or R_m the engineering ultimate tensile strength);

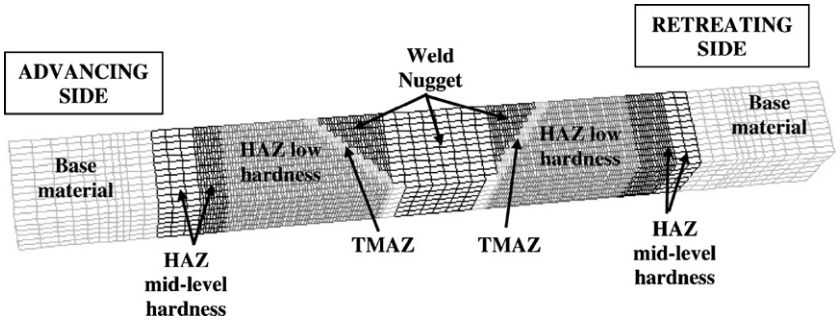

Fig. 3. Mesh and zones with different material properties for the modelling of the tensile behaviour of the hot weld (200 mm/min and 1000 rpm).

- the work hardening behaviour is described by a Voce law:

$$\frac{d\sigma_f}{d\varepsilon_p} = \theta - \beta(\sigma_f - \sigma_y), \tag{1}$$

which relates the work hardening rate $d\sigma_f/d\varepsilon_p$ – where σ_f is the flow stress and ε_p is the plastic strain – to the dislocation storage rate θ and the recovery rate β. The parameters θ and β are obtained by a linear fit on the variation of the strain hardening rate with the true flow stress in the region between the elasto-plastic transition and the localization (necking) stages. These two parameters are known as the Kocks–Mecking–Estrin parameters and they have been extensively used to describe the strain hardening of aluminium alloys [22–24].

3. Description of the FE model

In order to better understand the evolution of the complex stress and strain patterns during loading, the transverse tensile tests performed on the welded samples have been simulated using the general purpose finite element code ABAQUS [25] assuming J2 isotropic plasticity. A similar analysis has been performed by Lockwood and Reynolds [17]. The test sample is modelled using the local tensile properties measured with the micro-tensile specimens extracted in the different characteristic regions of the weld as depicted in Fig. 3 for the specific case of the transverse tensile test on the hot weld. The stress–strain curves were introduced point by point up to the onset of necking and have been extrapolated to larger strains using a Voce law (Eq. (1)). The position of the transition between the various regions of the welds and the inclination of these transitions are based on the hardness measurements (see Fig. 9) and the weld shapes observed on macrographs of the two welds. Due to the differences between the advancing and retreating sides of the weld, full 3D simulations had to be performed accounting only for one symmetry plane parallel to the loading direction and through thickness direction. The mesh is highly refined in the region where deformation localizes. Convergence studies have been conducted in order to ensure that the predicted local stress and strain evolution in that region of the weld were independent of the degree of mesh refinement up to large strains (typically equal to 1).

For each region of the weld, a series of three micro-tensile tests were available. The simulations were thus repeated three times for each weld in order to estimate the dispersion resulting from the experimental scatter.

4. Experimental and simulation results

4.1. TEM characterization

Fig. 4 shows the evolution of the fine hardening precipitates observed by transmission electron microscopy (TEM) in different zones of the weld. The base material in Fig. 4(a) contains a high density of fine hardening precipitates. Comparison of Fig. 4(a) and (b) shows that the heat-affected zone contains fewer but larger precipitates than the base material. The cross-section of the precipitates is more rounded than

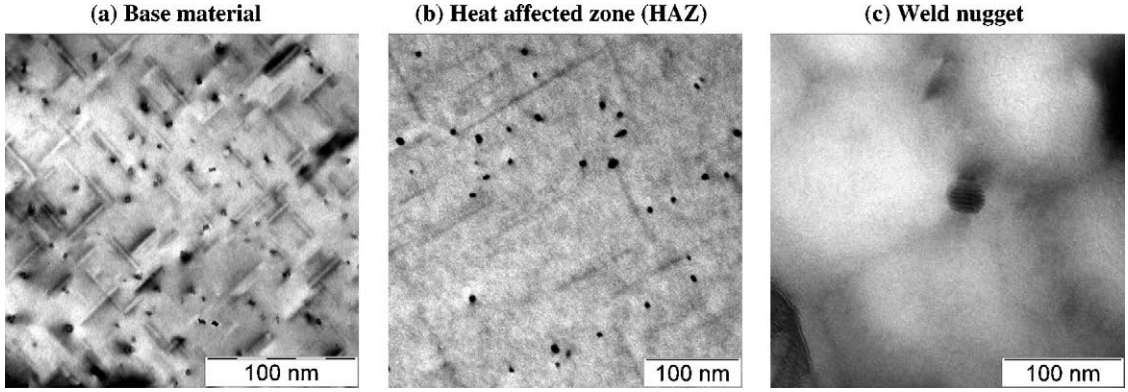

Fig. 4. Fine precipitation evolution in friction stir welds: (a) base material; (b) heat-affected zone (HAZ) of the hot weld (large β′ precipitates); (c) nugget of the cold weld (no β′ precipitates observed, dispersoïds are not dissolved). $[1\,0\,0]_{Al}$ zone axis.

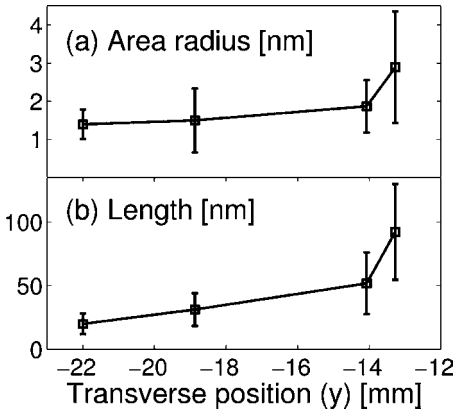

Fig. 5. TEM image analysis of the fine precipitates evolution in the hot (200 mm/min) weld; (a) mean precipitate area radius and (b) mean precipitate length.

rectangular which leads to the conclusion that these precipitates are β′ rather than B′ precipitates [5,26]. Precipitation is also dominantly homogeneous and thus not affected by the presence of the dispersoïds or dislocations. No TEM observations were performed in the TMAZ. Nevertheless, a high density of stored dislocations [27,28], associated to large strains, are anticipated in that region which could favour heterogeneous precipitation [15,19]. Fine precipitates are not observed in the nugget and the presence of dispersoïds demonstrates that they were not dissolved during welding (see Fig. 4(c)).

Fig. 5 shows the mean area radius and mean length of the fine precipitates as a function of the distance from the weld centre line in the hot weld. The mean area radius is defined as the radius of a circle having an area equal to the area of the observed precipitate. The precipitate length grows faster than the precipitate area radius with decreasing distance from the weld centre. This observation tends to confirm the identification of the heat-affected zone precipitates as β′ rather than β″ since β′ are semi-coherent with the aluminium matrix and hence tend to grow preferentially in the low coherency direction of the longest axis. The increasing size of the error bar in the heat-affected zone of the weld compared to the base material is due to a more widespread size distribution. This is consistent with the competition between two mechanisms in the heat-affected zone: the large precipitates present in the base material coarsen and the small ones dissolve. Fig. 6 shows the precipitates microstructure observed by TEM in the cold and the hot weld within the heat-affected zone at the location of the lowest hardness. The precipitates in the hot weld are nearly twice the size (length and area radius) of the precipitates in the cold weld.

4.2. DSC characterization

Fig. 7 presents typical DSC curves observed in the HAZ and weld nugget of a 6005A-T6 friction stir weld as compared to the base material. The identification of the peaks is based on a literature survey [4–7,29] and on the results presented in Fig. 7:

- the GP zone dissolution peak is identified at 200–220 °C;
- the β″ dissolution or precipitation peak is identified at around 250–270 °C;

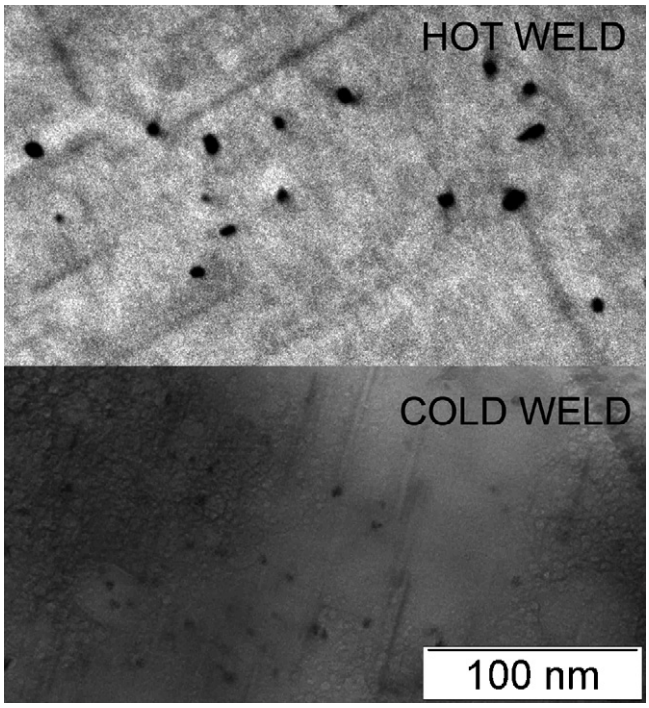

Fig. 6. Fine precipitation in the heat-affected zone of two friction stir welds with a rotational speed of 1000 rpm. The hot weld has an advancing speed of 200 mm/min and the cold weld has an advancing speed of 1000 mm/min. $[1\,0\,0]_{Al}$ zone axis.

- the β′ precipitation peak is identified at around 290–310 °C;
- the β(Mg_2Si) precipitation peak is identified at 460–470 °C;
- the β(Mg_2Si) dissolution peak is identified at around 500–510 °C;
- some Si precipitation peaks can be found at various temperatures ranging from 300 to 450 °C.

The exact position of the maximum of dissolution or precipitation peaks is dependent on the size of the precipitates. β′ precipitates can be formed directly from β″ precipitates without going through a dissolution stage.

4.2.1. Base material

The base material DSC curve shows a large dissolution peak at around 260 °C due to the dissolution of the β″ initially present

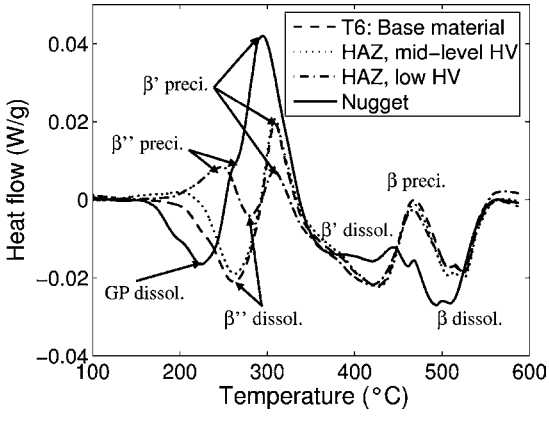

Fig. 7. DSC curves of different zones in the cold weld (HV = Vickers hardness).

in the T6 state. At higher temperatures, the DSC shows β′ precipitation at about 310 °C, followed by a broad β′ dissolution peak from 350–420 °C, and then a precipitation peak at about 475 °C associated with the β(Mg_2Si) phase. The β(Mg_2Si) precipitates will finally dissolve before the material melts.

4.2.2. HAZ with mid-level hardness

The main differences between this curve and the base material curve are a small broad precipitation peak at around 200 °C that is associated with GP zone precipitation, and slightly less β″ dissolution. It seems logical to conclude that the observed GP zone precipitation during the DSC results from a supersaturated solution caused by the dissolution of part of the β″ precipitates during the welding process. The GP zone dissolution peak is most probably convoluted with the β″ dissolution peak. The DSC spectra is virtually unchanged with respect to the base material from about 300 °C, and shows β′ precipitation, followed by β′ dissolution, β precipitation and β dissolution.

4.2.3. HAZ with low hardness

The measured DSC curve is very different than in the base material, especially with respect to the β″ and β′ peaks. In the low hardness HAZ, a β″ precipitation peak is observed at 250 °C, and the β′ precipitation peak at 310 °C is significantly reduced. The β″ precipitation peak in that zone of the weld is consistent with the existence of a supersaturated solid solution. The lower area under the β′ peak indicates that some β′ were already present and/or that the dissolution of β″ available for β′ is incomplete. This region of the weld involves β′ precipitates in a supersaturated solid solution. This result is consistent with our TEM observations of Fig. 4(b), which show long rod-shaped precipitates that are presumably semi-coherent β′ precipitates. The presence of a supersaturation in solid solution is consistent with our post-welding heat treatments hardness measurements described later (Fig. 9). Note also that the presence of both large precipitates and a fair amount of supersaturation has been suggested by a thermodynamically based microstructure model [30].

4.2.4. Nugget

Fig. 7 shows that the DSC curve associated to a sample extracted from the weld nugget presents a large first dissolution peak attributed to the dissolution of the GP zones. GP zones have thus precipitated in the weld nugget due to natural aging. A large β′ precipitation peak follows the GP zone dissolution peak, with an indication of β″ precipitation associated with the shoulder on the curve at about 260 °C. Such large β″ and β′ precipitation peaks are expected in a sample with a high solid solution concentration (which led to GP zones formation by natural aging). The DSC curve is also very different than the other curves at higher temperatures. The lower β(Mg_2Si) precipitation peak and the larger β(Mg_2Si) dissolution peak can be explained by the precipitation of β(Mg_2Si) in the weld nugget.

Table 2
Tensile properties of the base aluminium alloy 6005A-T6

Direction of loading	Extrusion	Long transverse
Yield strength at 0.2%, σ_y (MPa)	265.6 ± 2.2	255.5 ± 0.7
Ultimate tensile strength, R_m (MPa)	287.8 ± 1.2	276.8 ± 0.7
True strain at necking, ε_u	0.086 ± 0.001	0.078 ± 0.002
Dislocation storage rate, θ (MPa)	918 ± 29	806 ± 4
Recovery rate, β	11.8 ± 0.4	10.1 ± 0.3

4.3. Mechanical properties

Table 2 summarizes the tensile properties of the base material. The yield strength in the extrusion direction is 4% higher than in the long transverse direction. The ductility defined by the true uniform strain at necking is also slightly larger in the extrusion direction.

Table 3 summarizes the properties derived from the transverse tensile tests performed on the welds. The cold weld has a larger strength than the hot weld by about 6% but a lower engineering strain at maximum load (6.6% instead of 7.8%). Fig. 8 compares the results of the local tensile strains, determined from the digital image correlation (DIC) at mid-thickness, for the two welding conditions when the global elongation is equal to 1.4 times the engineering strain at maximum load. At this level of global deformation, plastic strains localize within the heat-affected zone in both welds, and always on the retreating side. The deformation in the nugget is larger in the cold weld than in the hot weld.

Fig. 9 presents the variation of the hardness as a function of the position along a transverse weld section in the hot and the cold welds both before and after a post-welding heat treatment. Similar trends are observed for both welds. The hardness after welding and natural aging for more than 1 year exhibits a drop in the heat-affected zone and has a similar level across the TMAZ and weld nuggets. The post-welding heat treatment has only a minor effect on the hardness of the base material (evidenced in Fig. 9, cold weld) but leads to significant recovery

Table 3
Measured and predicted transverse tensile properties of the welds

Weld	Hot		Cold	
	Experiment	Model	Experiment	Model
Yield strength at 0.1%, R_p (MPa)	105	126 ± 2.4	113	127 ± 2.3
Pseudo-ultimate tensile strength, R_m (MPa)	193	192 ± 4.1	202	213 ± 5.4
Engineering strain under maximum load, e_u (%)	7.8	5.8 ± 0.8	6.6	6.8 ± 0.4
Distance y of fracture from the weld centre (mm), or position where deformation localizes in the model	11.8	−12.6 ± 0.80	5.7	7.4 ± 0.23

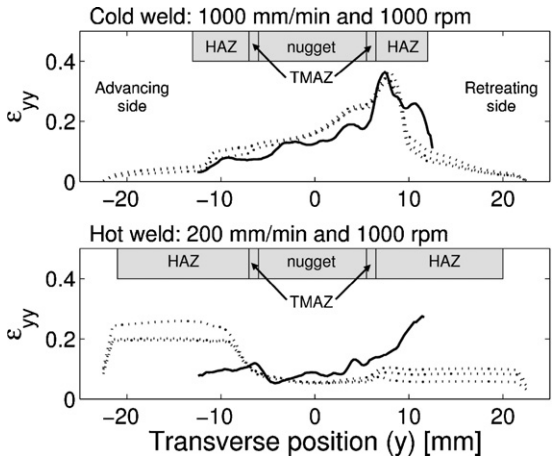

Fig. 8. Comparison of the predicted (doted lines) and measured (DIC results, solid line) distribution of local strains in the tensile direction ε_{yy} at mid-thickness when the engineering strain for the cold and hot weld is equal to 1.4 times its value under maximum load (from Table 3). The width of the various weld zones at mid-thickness is sketched over each plot.

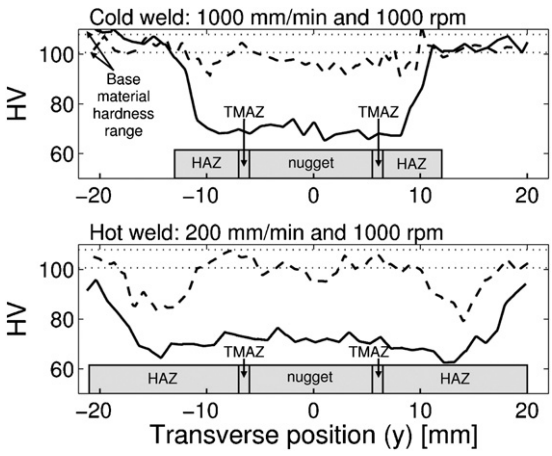

Fig. 9. Evolution of the hardness in the as welded condition (solid line) and after a post-welding heat treatment (dashed line) as a function of the position along a transverse section of the weld. Comparison of a hot (200 mm/min) and a cold (1000 mm/min) weld. The width of the various weld zones at mid-thickness is sketched under each plot. The base material hardness range of 104.2 ± 3.6 HV is indicated by two vertical lines.

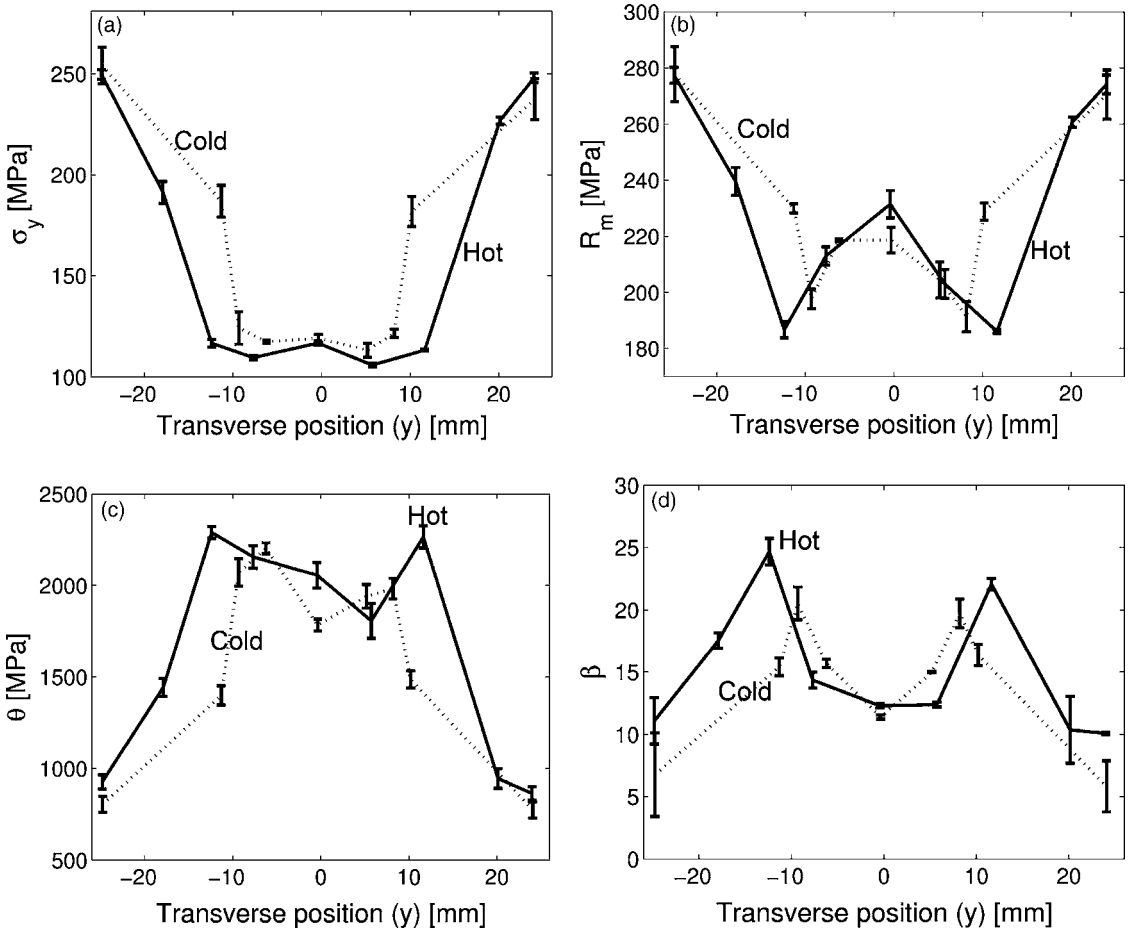

Fig. 10. Evolution of the local tensile properties as a function of the position along a transverse section of the weld. Comparison of a hot (200 mm/min) and a cold (1000 mm/min) weld. Error bars indicate the standard deviation for three samples in each weld zone. (a) Yield strength σ_y; (b) ultimate tensile strength R_m; (c) rate of dislocation storage θ; (d) dynamic recovery rate β.

of the hardness of the weld nugget. The hardness in a portion of the heat-affected zones does not return to the initial base material hardness (104.2 ± 3.6 HV). This effect is much more pronounced for the hot weld than for the cold weld. The hardness in the weld nugget does not seem to be fully recovered especially in the cold weld.

Fig. 10 presents the tensile properties measured on microtensile specimens extracted in the different zones of the weld in the as welded condition after natural aging for more than 1 year as a function of the distance from the weld centreline: (a) yield strength, (b) ultimate tensile strength, (c) θ hardening rate factor, and (d) β recovery rate factor (the θ and β parameters were obtained by a linear fit, see Eq. (1)). Again, the representative values for the base material are provided in Table 2. The base material has the lowest strain hardening capacity and the highest yield and ultimate tensile strength. The heat-affected zone in the low strength and low hardness region also has a low strain hardening capacity, as evidence by a high recovery rate β. The higher value of the recovery rate β in the HAZ of the hot weld compared to the same zone in cold weld explains why the HAZ of the hot weld exhibits a lower ultimate tensile strength than in the cold weld. The hardness and yield strength of the weld nugget and the HAZ are similar in the cold weld, while they are slightly higher in the nugget of the hot weld. The main difference between the HAZ and the nugget results from the difference in strain hardening capacity; the nugget presents a much higher strain hardening capacity, as evidenced by a high dislocation storage rate θ but a much lower recovery rate β than the HAZ. The difference in recovery rate between the base material and the HAZ is due to the coarsening of β' precipitates in that region of the weld (see Ref. [30] for more comments). Hence, the ultimate tensile strength in the nugget is significantly larger than in the HAZ.

4.4. FE simulation of the macroscopic transverse tensile behaviour

The results of the FE simulations of the tensile test performed transverse to the welds are compared in Fig. 8 to the experimental DIC results at the same applied displacement. Table 3 compares the predicted and measured tensile properties. The agreement is reasonable considering the approximation introduced by using constant properties throughout each region of the weld, whereas, the actual properties present smoother gradients (see for example the hardness curve in Fig. 9). Possible reasons for the discrepancies will be discussed further. The comparison for the cold weld is excellent. For the hot weld, the FE simulation predicts strain localization on the advancing side rather than the retreating side (see also Table 3).

5. Discussion

5.1. Microstructural evolution versus hardness and yield strength

The microstructure evolution inferred from the TEM and DSC analyses provide the keys for rationalizing the variations of the hardness and yield strength through the weld. The decrease of hardness and yield strength observed in the HAZ toward the weld centre are related to the coarsening and/or dissolution of the initial precipitates and their progressive transformation into the semi-coherent β' phase. The yield strength evolution of precipitate strengthened alloys can be explained by two different precipitates/dislocation interaction mechanisms. If the precipitates are small (typically < 3–5 nm [30,31]) they are sheared by the dislocations and the yield strength of the material is proportional to $\sqrt{f_v r}$, where f_v is the precipitates volume fraction and r is the mean precipitate radius. If the precipitates are larger (typically > 3–5 nm [30,31]), they are bypassed by the dislocations while leaving a closed dislocation loop (Orowan mechanism), in this case, the yield strength of the material is proportional to $\sqrt{f_v}/r$. The hardness of these alloys is proportional to their yield strength, neglecting strain hardening effect on the hardness. The HAZ presents the lowest yield strength and hardness. The microstructure of this region is characterized by the dissolution of the initial β'' precipitates and the presence of β' precipitates. The much lower yield strength observed in the HAZ can be related to the Orowan mechanisms in an alloy with a low volume fraction of large precipitates compared to the base material in T6 state that has a maximum volume fraction of shearable precipitates.

The high temperatures (around 500 °C [20]) in the weld nugget cause the dissolution of the β'' precipitates in that region of the weld. No fine precipitates are observed in this zone, although the DSC results are consistent with the presence of GP zones. Hence, the hardness of the nugget is similar or slightly superior to the hardness of the HAZ even though the strengthening is caused by different microstructure-based strengthening mechanisms.

A post-welding heat treatment (PWHT) constitutes an indirect method for evaluating the solid solution content and the possible supersaturation. Recovering the initial hardness through PWHT implies that the region was supersaturated in solid solution and/or was containing GP zones, which form β'' during PWHT. The results of Fig. 9 can be interpreted as follows:

- Since the hardness in the "medium-hardness" portion of the HAZ is partially recovered after the PWHT, it suggests that β'' precipitates were partially dissolved in that region of the weld. This is consistent with the conclusion drawn from the analysis of the DSC curves.
- The precipitation of large β' in the HAZ leads to a decrease of the amount of solid solution available for re-precipitation of β'' during the PWHT, hence the drop of hardness in the HAZ close to the weld centre (initially the "low hardness" HAZ region) is not completely recovered after PWHT.
- The hardness in the nugget does not seem to be fully recovered. Indications of another precipitation than GP zones in the weld nugget, presumably $\beta(Mg_2Si)$, has been found by DSC and SEM observations but still needs confirmation, see also Gallais [19] in the case of AA6056 friction stir welds. This is consistent with the incomplete hardness recovery after PWHT in the weld nugget. The precipitation of $\beta(Mg_2Si)$ will indeed decrease the amount of magnesium and silicon left in solid solution. Furthermore, considering that the cooling

rate in a weld is slow compared to a quench from a solution treatment, vacancy depletion might occur, resulting in non-optimum precipitate nucleation and the inability to obtain T6 hardness.

5.2. Microstructure versus strain hardening capacity

The analysis of the variations of the parameters β and θ provides insight into the physical mechanisms at the origin of the difference in strain hardening behaviour between the various zones of the welds in relation to the microstructure [30,32]. The strain hardening parameter θ is associated to the rate of dislocation storage. This parameter reaches its lowest value when all alloying elements have precipitated in small precipitates, which can be sheared by the dislocations [33]. A supersaturation in solid solution is known to increase the dislocation storage rate θ, although the underlying mechanism is not well established. Deformation induced precipitation, i.e. dynamic precipitation [34], or the enhanced formation of dislocation forest junctions in the presence of solute atoms have been proposed. On the other hand, if the precipitates are too large to be sheared by dislocations, Orowan loops accumulate around the precipitates. The formation of these Orowan loops for medium sized precipitates (still coherent with the matrix [30]) results in a drastic increase of the dislocation storage rate θ ([30] and Ref. therein). Therefore, if the precipitate size increases, the dislocation storage rate θ increases as well, at least for medium sized precipitates. The strain hardening parameter β is associated to the recovery rate. It is mainly affected by the presence of Orowan loops, which tend to drastically increase the recovery rate. The presence of Orowan loops favours the partial and local annihilation of dislocations owing to the long range back stress favouring the change of gliding plane and leading to larger effective recovery rates [30].

The values of the strain hardening parameters θ and β in the different zones of the weld are given in Fig. 10(c) and (d). The base material contains the highest density of small shearable β'' precipitates which explains the low levels of both θ and β. The heat-affected zone consists of large β' precipitates, which are presumably storing Orowan loops. Hence, the HAZ presents much higher values of θ and β. The weld nugget contains GP zones and eventually some alloying element left over in solid solution, which do not have sufficient supersaturation driving force to precipitate naturally. The recovery rate is only weakly affected by the presence of elements in solid solution and GP zones.

5.3. Effect of the advancing speed on the microstructure and local tensile properties

The hardness results presented in Fig. 9 shows that some portions of the HAZ in the hot weld (welding speed = 200 mm/min) have a lower hardness recovery after PWHT than for the cold weld (welding speed = 1000 mm/min). This implies more precipitate coarsening in the hot weld and indicates that the solid solution concentration in the HAZ is thus lower in the hot weld than in the cold weld.

The hardness in the HAZ before PWHT (but after natural aging) is lower in the hot weld than in the cold weld. This can be explained by the lower precipitate density associated with the larger precipitates (see TEM micrographs of Fig. 6) giving a lower hardness in the HAZ of the hot weld. Furthermore, the higher solid solution concentration in the HAZ of the cold weld favours natural aging and hardening in that region. These two effects explain why the HAZ has a hardness not much lower than in the weld nugget, especially in the cold weld.

The two welds also show differences in the strain hardening capacity. The recovery rate β and the rate of dislocation storage θ are larger in the HAZ of the hot weld than in the cold weld, see Fig. 10(c) and (d). This is again consistent with the larger precipitate size in the heat-affected zone of the hot weld (see Fig. 6). As a consequence of the distribution of the strain hardening parameters θ and β in the heat-affected zone and the weld nugget, the ultimate tensile strength of the heat-affected zone of the hot weld is lower than in the cold weld.

5.4. Global behaviour of friction stir welds

The transverse yield strength of a weld is controlled by the yield strength of the weakest zone of the weld (i.e. the HAZ). This is the case in this study if one takes anisotropy into account. Indeed a difference of about 10 MPa between the HAZ yield strength and the weld yield strength is observed in both welds, corresponding to the difference in yield strength between the longitudinal and transverse directions of the base material (reported in Table 2). This moderate anisotropy in the tensile properties of the base material also partially explains that the yield strength is overestimated by the finite element model which uses properties from the micro-tensile samples extracted in the longitudinal direction (also the welding and extrusion direction) to predict properties in the transverse long direction (direction of the standard transverse tensile tests on the welds). The lower yield strength of the hot weld compared to the cold weld is due to the lower yield strength of the heat-affected zone of the hot weld. Hence, increasing the weld transverse yield strength requires increasing the solid solution concentration to favour GP zones formation in the heat-affected zone and decreasing the precipitate size in that region of the weld. These conditions could be achieved by increasing the advancing speed or imposing local post-welding heat treatments.

At larger strains, deformation localizes in the HAZ, close to the TMAZ in the cold weld (see Fig. 8) and final fracture will finally occur in the HAZ. The localization of the deformation in the HAZ, rather than in the entire joint as could be deduced from the hardness measurements, is due to the larger strain hardening capacity of the weld nugget and the TMAZ compared with the HAZ. This can also be deduced from the values of the ultimate tensile strength of the different zones of the weld, see Fig. 10(b). The local deformation of the nugget of the cold weld at large global deformations is larger than in the hot weld (see Fig. 8). This is consistent with the smaller strength mismatch between the weld nugget and the HAZ in the cold weld than in the hot weld, see Fig. 10(b). This difference in localization behaviour will undoubtedly affect the final global elongation of the welds,

but the difference in width of the localized band does not allow to draw simple conclusions by any other means than a simulation of the whole weld based on the local tensile properties.

The trend showing an increase of the ultimate tensile strength of the welds with increasing advancing speed (see Table 3) can be attributed to the lower recovery rate parameter β in the heat-affected zone of the cold weld than in the hot weld. Consequently, the microstructure obtained in the HAZ of cooler welds does not only increase the yield strength but also decreases the HAZ recovery rate and hence increases the strength of the weld. The slight overestimation in the prediction of the ultimate tensile strength for the cold weld can be attributed to the anisotropy in the tensile properties, to the fact that damage is not taken into account, and to unrealistically steep gradients of properties between the different regions of the weld. These reasons can also be invoked to explain the underestimation of the strain at maximum load in the hot weld as well as the difference between the predicted and measured local deformation in Fig. 8.

The location of the fracture zone in the two friction stir welds (see Table 3) corresponds to the position of the minimum ultimate tensile strength of both welds, i.e. in the HAZ. It is further away from the weld centreline when the welding speed decreases since the width of the HAZ increases with decreasing advancing speed (see Fig. 9). The region where deformation localizes at large strains is predicted to occur on the retreating side of the welds (positive position) for the cold weld while for the hot weld it is predicted on the advancing side (negative position) (see Fig. 8). In practice, fracture of the two friction stir welds always occurred on the retreating side. Thermocouple measurements [20] have shown that the temperature asymmetry is larger in cold welds than in hot welds with a clearly hotter advancing side in cold welds, and a much less clear situation in hot welds. In the hot weld, the localization of fracture can vary with very slight differences in shape and tensile properties of the weld zones, which are not captured by the model. A slight perturbation of the initial condition modifies the side where plastic deformation localizes. In the cold weld, fracture occurs on the coldest side of the weld and this can be explained by the fact that the higher temperatures on the advancing side favour a more complete precipitate dissolution and hence a higher strength after natural aging.

6. Conclusions

The flow properties of two friction stir welds generated using two different advancing speeds have been analyzed based on an experimental characterization campaign of the state of precipitation, of the local and global mechanical tests and on FE simulations.

- Dissolution of the β'' precipitates and formation of coarse β' precipitates occur in the heat-affected zone (HAZ) within the "mid-level hardness" region. The size of the β' precipitates in the hot weld (low advancing speed) is larger than in the cold weld (high advancing speed) and the solid solution concentration in the HAZ in the low hardness region is lower in the hot weld. As a consequence, the hardness and yield strength of the heat-affected zone of the hot weld are lower than in the cold weld. The recovery rate and the dislocation storage rate are both high in the heat-affected zone which is consistent with the formation of Orowan loops when the dislocations interacts with the large semi-coherent β' precipitates. Both strain hardening parameters are higher in the hot weld due to the increase in β' precipitate size with decreasing advancing speed.
- No fine precipitates are observed by TEM in the weld nugget. DSC measurements are consistent with GP zone formation in that region, leading to an increase of yield strength compared to the yield strength of the same alloy under a supersaturated solid solution. The weld nugget has a high apparent dislocation storage rate due to dynamic precipitation [30,34] and a rather low recovery rate since no large precipitates favouring dislocation de-localization are present in that region of the weld.
- The transverse tensile properties of the weld depend on the properties of the different zones of the weld. The hardness is not the sole property governing the global behaviour during transverse tensile testing since it is not significantly different in the nugget and in the heat-affected zone. The strain hardening capacity of the weld centre is larger than that of the heat-affected zone, and thus fracture occurs in the heat-affected zone of the weld.

Acknowledgements

The authors are grateful to Brian Wirth for his valuable comments. Aude Simar acknowledges the financial support of FRIA Belgium and FSR-UCL. This research was also carried out under the University Attraction Poles (IAP) Programme Phase 6–24, financed by the Belgian State, Federal Office for Scientific, Technical and Cultural Affaires. The authors acknowledge the help of Marc Sinnaeve and the staff of the PRM workshop for the tensile tests, Liliane Rolly for the DSC measurements, Sophie Ryelandt for the DIC measurements and Laurence Ryelandt for the TEM observations. The company Sapa RC Profile, Ghlin, Belgium is gratefully acknowledged for providing the materials of this study.

References

[1] (a) W.M. Thomas, E.D. Nicholas, J.C. Needham, M.G. Murch, P. Templesmith, C.J. Dawes, GB Patent Application No. 9125978.8. (December 1991).;
(b) W.M. Thomas, E.D. Nicholas, J.C. Needham, M.G. Murch, P. Templesmith, C.J. Dawes, US Patent No. 5,460,317. (October 1995).

[2] G. Liu, L.E. Murr, C.S. Niou, J.C. Mc Clure, F.R. Vega, Scripta Mater. 37 (1997) 355–361.

[3] J.Q. Su, T.W. Nelson, R.S. Mishra, M.W. Mahoney, Acta Mater. 51 (2003) 713–729.

[4] I. Dutta, S.M. Allen, J. Mater. Sci. Lett. 10 (1991) 323–326.

[5] G.A. Edwards, K. Stiller, G.L. Dunlop, M.J. Couper, Acta Mater. 46 (11) (1998) 3893–3904.

[6] W.F. Miao, D.E. Laughlin, Scripta Mater. 40 (7) (1999) 873–878.

[7] A.K. Gupta, D.J. Lloyd, S.A. Court, Mater. Sci. Eng. A 301 (2000) 140–146.

[8] C. Gallais, A. Simar, D. Fabrègue, A. Denquin, G. Lapasset, B. de Meester, Y. Bréchet, T. Pardoen, Metall. Mater. Trans. A 38 (5) (2007) 964–981.

[9] D. Lassance, D. Fabregue, F. Delannay, T. Pardoen, Prog. Mater. Sci. 52 (2007) 62–129.
[10] Y.S. Sato, H. Kokawa, M. Enmoto, S. Jogan, Metall. Mater. Trans. A 30 (1999) 2429–2437.
[11] W.B. Lee, Y.M. Yeon, S.B. Jung, Mater. Sci. Technol. 19 (2003) 1513–1518.
[12] Y.S. Sato, H. Kokawa, M. Enmoto, S. Jogan, T. Hashimoto, Metall. Mater. Trans. A 30 (1999) 3125–3130.
[13] A. von Strombeck, J.F. dos Santos, F. Torster, P. Laureano, M. Koçak, Proceedings of the 1st International Symposium, FSW, Thousand Oaks, CA, USA, 1999.
[14] Y.S. Sato, S.H.C. Park, H. Kokawa, Metall. Mater. Trans. A 32 (2001) 3023–3031.
[15] A. Denquin, D. Allehaux, M.-H. Campagnac, G. Lapasset, Weld. World 46 (2002) 14–20.
[16] W.D. Lockwood, B. Tomaz, A.P. Reynolds, Mater. Sci. Eng. A 323 (2002) 348–353.
[17] W.D. Lockwood, A.P. Reynolds, Mater. Sci. Eng. A 339 (2003) 35–42.
[18] M. Cabibbo, E. Meccia, E. Evangelista, Mater. Chem. Phys. 81 (2003) 289–292.
[19] C. Gallais, PhD Thesis, Institut National Polytechnique de Grenoble, France, 2005.
[20] A. Simar, T. Pardoen, B. de Meester, Sci. Technol. Weld. Join. 12 (4) (2007) 324–333.
[21] "Demi-produits aluminium": Pechiney Rhenalu, 1997.
[22] D. Chu, J.W. Morris, Acta Mater. 44 (7) (1996) 2599–2610.
[23] S. Esmaeili, L.M. Cheng, A. Deschamps, D.J. Lloyd, W.J. Poole, Mater. Sci. Eng. A 319–321 (2001) 461–465.
[24] L.M. Cheng, W.J. Poole, J.D. Embury, D.J. Lloyd, Metall. Mater. Trans. A 34A (2003) 2473–2481.
[25] ABAQUS, Version 6.3, 2002, User's Manual, Hibbit, Karlsson and Sorensen, Providence, RI.
[26] S.D. Dumolt, D.E. Laughlin, J.C. Williams, Scripta Metall. 18 (1984) 1347–1350.
[27] M. Strangwood, C.L. Davis, M.M. Attallah, Proceedings of the 5th International Symposium, FSW, Metz, France, 2004.
[28] C. Genevois, A. Deschamps, A. Denquin, B. Doisneau-Cottignies, Acta Mater. 53 (8) (2005) 2447–2458.
[29] A.K. Gupta, D.J. Lloyd, S.A. Court, Mater. Sci. Eng. A 316 (2001) 11–17.
[30] A. Simar, Y. Bréchet, B. de Meester, A. Denquin, T. Pardoen, Acta Mater. (2007), in press.
[31] O.R. Myhr, O. Grong, S.J. Andersen, Acta Mater. 49 (2001) 65–75.
[32] A. Simar, PhD Thesis, Universite Catholique de Louvain (UCL), Belgium, 2006.
[33] Y. Estrin, A.S. Krausz, K. Krausz (Eds.), Academic Press, San Diego, (1996) 69–106.
[34] A. Deschamps, M. Nieuwczas, F. Bley, Y. Brechet, J.D. Embury, L. Le Sinq, F. Livet, J.P. Simon, Phil. Mag. A 79 (10) (1999) 2485–2504.